**Development of New Generation Reduced Activation Ferritic-Martensitic Steels for Advanced Fusion Reactors** †

L. Tan[1*], L.L. Snead[2], Y. Katoh[1]

[1] Oak Ridge National Laboratory, Oak Ridge, TN 37831, USA

[2] Massachusetts Institute of Technology, Cambridge MA 02139, USA

[*] Corresponding author: One Bethel Valley Road, P.O. Box 2008, MS-6136, Oak Ridge, TN 37831; Phone: +1-865-574-4628; E-mail: tanl@ornl.gov (L. Tan)

**Abstract**

International development of reduced activation ferritic-martensitic (RAFM) steels has focused on 9 weight percentage Cr, which primarily contain $M_{23}C_6$ (M=Cr-rich) and small amounts of MX (M=Ta/V, X=C/N) precipitates, not adequate to maintain strength and creep resistance above ~500°C. To enable applications at higher temperatures for better thermal efficiency of fusion reactors, computational alloy thermodynamics coupled with strength modeling have been employed to explore a new generation RAFM steels. The new alloys are designed to significantly increase the amount of MX nanoprecipitates, which are manufacturable through standard and scalable industrial steelmaking methods. Preliminary experimental results of the developed new alloys demonstrated noticeably increased amount of MX, favoring significantly improved strength, creep resistance, and Charpy impact toughness as compared to current RAFM

steels. The strength and creep resistance were comparable or approaching to the lower bound of, but impact toughness was noticeably superior to 9–20Cr oxide dispersion-strengthened ferritic alloys.

*Keywords:* Precipitates; Strengthening; Toughness; ODS ferritic steel; Reduced activation ferritic-martensitic steels

## 1. Introduction

Reduced activation ferritic-martensitic (RAFM) steels for fusion reactor structural applications have been under development for about three decades. These steels have converged to a nominal 9 weight percentage (wt%) Cr content, largely because this minimizes the radiation-induced ductile-brittle transition temperature (DBTT) shift compared to steels with either lower or higher Cr content [1]. The goals implied for a *reduced activation material,* complying with waste disposal and materials recycle limits, require alloying elements Mo and Nb generally used in conventional FM steels such as Grade 91 and Grade 92 [2] be replaced by W and Ta. There are also restrictions on the content of other alloying elements (e.g., Ni, Co, etc.) and impurities (e.g., Ag, Al, etc.) in RAFM steels [3].

Current versions of RAFM steels such as F82H and Eurofer97 exhibit comparable tensile properties, though appreciably lower creep resistance than similar engineering alloys such as Grade 91. Recovery of lath boundaries and cell/packet structures occurred during creep tests, resulting in the softening of the materials during creep [4]. Unfortunately, the presence of the relatively large amount of $M_{23}C_6$ (M = Cr-rich) precipitates, up to ~1.9 volume percentage (vol%,

calculated) in F82H, primarily at prior-austenite grain and cell/packet boundaries cannot effectively pin the grain boundaries during creep due to their easy coarsening to > ~200 μm from initial ≤ 100 nm. In contrast, MX-type (M = Nb/Ta/V, X = C/N) nanoprecipitates, usually with a size of ~50 nm, have been shown to provide excellent stability at similar temperatures [5,6], but only limited amounts of MX nanoprecipitates are present in current RAFM steels, e.g., calculated to be ~ 0.12 vol% in F82H, well below the ~0.35 vol% (calculated) in Grade 91. The low density of MX precipitates provide little grain boundary pinning, hence the lower creep resistance of RAFM as compared to Grade 91.

In addition to RAFM steels, oxide dispersion-strengthened (ODS) alloys, also named as nanostructured ferritic alloys (NFA) recently, with Cr content generally in the range of 9~20 wt% are also being developed for fusion and other applications. Unlike RAFM steels manufactured using traditional industrial scale vacuum induction melting (VIM) and remelting techniques such as electro-slag remelting (ESR) and vacuum arc remelting (VAR), the NFA/ODS alloys are fabricated by complex mechanical alloying (MA) steps, then hot consolidation, as schematically shown in Fig. 1 [7]. MA enables the incorporation of large amount of oxide nanoclusters. The predominant small oxide nanoclusters (< 10 nm in size) in NFA/ODS alloys have been reported in the range from ~0.7 vol% in ODS-Eurofer (9Cr: nanoclusters of ~5 nm and $1.2\times10^{23}$ $m^{-3}$ [8]) to ~1 vol% in PM2000 (20Cr: ~20 nm and $2.5\times10^{21}$ $m^{-3}$ [9]) and ~3 vol% in 14YWT (14Cr: ~3 nm and $2\times10^{24}$ $m^{-3}$ [10]).

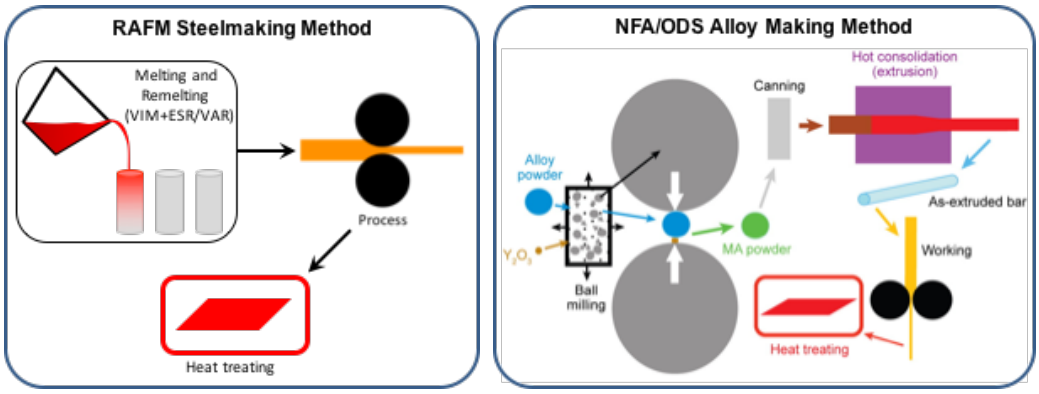


Fig. 1. Schematic manufacture routes of RAFM steels and NFA/ODS alloys [7].

The extremely large amount of oxide nanoclusters in NFA/ODS alloys effectively pin the sub-micrometer ferritic grains, leading to superior creep resistance of these alloys. The oxide nanoclusters also potentially help radiation resistance and helium management, by acting as sink/trapping sites for irradiation produced defects and helium atoms. As shown in Fig. 2 (adapted from [11]), the increase of sink strength, primarily contributed by the increased amount of nanoparticles in going from Eurofer97 to ODS-Eurofer and 14YWT, noticeably decreases radiation hardening at 250 and 300°C. Despite the high strength and radiation resistance advantages of NFA/ODS alloy, the MA production of NFA/ODS alloys results in high fabrication cost, small volume of products, limitations on the complexity of the final product, and a high likelihood of mechanical property anisotropy and low toughness. RAFM steels have approximately the opposite features compared to NFA/ODS alloys, as summarized in Fig. 2. As suggested in Fig. 2, a class of advanced RAFM steels, called castable nanostructured alloys (CNAs), is between RAFM and NFA/ODS alloys in capturing the positive engineering attributes of each alloy system for nuclear applications. The CNAs are manufactured using the traditional industrial scale steelmaking methods used for RAFM steels, favoring flexible product forms such as forgings, plates, pipes, tubes, as well as castings as the ASTM standardized Grade 91. The

CNAs contain a significantly increased amount of MX nanoprecipitates, leading to superior properties embracing the merits of current RAFM steels and NFA/ODS alloys.

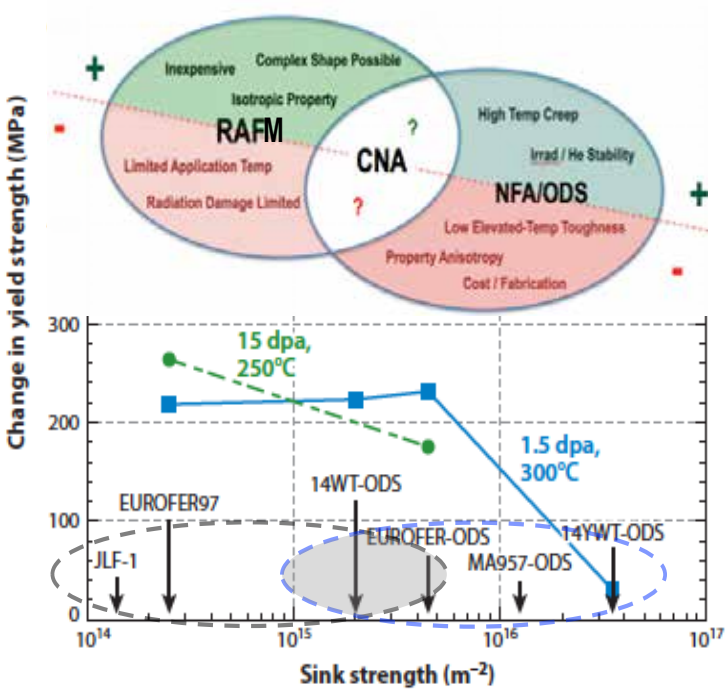


Fig. 2. Position of CNA compared to RAFM and NFA/ODS alloys (adapted from [11]).

## 2. Alloy Microstructural Design

Two routes were explored for increasing the amount of MX nanoprecipitates in CNAs. One is the generally pursued route of increasing V, Ta, and N content to form (V,Ta)N. The other is to include Ti and restrict N, which favors carbide formation, e.g., (Ti,Ta)C. The amount of $M_{23}C_6$ is also reduced, which is expected to improve yield strength and creep resistance [12,13]. As the austenite stabilizers are limited to C, N, and Mn in RAFM/CNA steels, the content of other alloy elements such as Cr, W, Ta, V, Si, and Ti (all ferrite stabilizers) was balanced using computational alloy thermodynamics. The initial composition of CNAs in wt% is targeted to be in the range of 8.3–9.0 Cr, 1.0–1.5 W, <1.0 Mn, 0.1–0.3 V, 0.05–0.15 Ta, <0.2 Ti, <0.2 Si, 0.08–0.15 C, <0.06 N

with the balance Fe. The content of each alloying element has been guided by the results of computational alloy thermodynamics, together with literature findings. For instance, increasing W had a more beneficial effect on fatigue life compared with increasing Ta [14]. Increasing W content to 0.7 wt% was found to reduce minimum creep rate [15], going to 2 wt% increased DBTT [16,17], and further increases to 3 wt% and beyond would have the undesirable effect of stabilizing δ-ferrite and favoring more $Fe_2W$ Laves phase formation [18,19]. Increasing Ta in the range of 0.06–0.15 wt% reduced the prior-austenite grain size and favored small spherical (Ta,V)(C,N) precipitates [20,21,22]. However, the higher Ta content deteriorated creep-fatigue resistance with increasing W [23]. Increasing Si generally decreased prior-austenite grain size and favored Laves phase formation [24,25]. Impact toughness was improved by the refined grains, but decreased significantly when Si content exceeded 0.22 wt% due to pronounced Laves phase formation [24].

Figure 3 shows an example of alloy design using computational alloy thermodynamics coupled with strength modeling. Computational alloy thermodynamics calculations were conducted with Pandat software [26] with the in-house developed OCTANT database [27]. The calculated temperature-dependent phase mole fractions in Fig. 3a show the precipitate phases in two CNAs and are compared to Eurofer97. To have better readability, the precipitate phases in the CNA3 (similar to those in the CNA2) and the predominant phases (i.e., ferrite [α and δ], austenite [γ] and liquid from low to high temperatures) in the alloys are not included in the plot. The CNA1, with a chemical composition listed in Table 1, is primarily strengthened by MN, e.g., (V,Ta)N, which was developed following the outline of Klueh [28] and related studies [22,29]. In contrast, the CNA2 and CNA3 (Table 1) are primarily strengthened by MC, e.g., (Ti,Ta)C. These new alloy compositions favor the formation of larger amounts of MX in the CNAs than found in Eurofer97.

Unlike the stable MC in the CNA2 and CNA3, MN in the CNA1 and Eurofer97 undergoes a sluggish phase transformation into Z-phase, primarily in the form of CrTaN, at temperatures below ~750°C. The coarse Z-phase consumes fine MN during long-term tests and services, so is expected to impair the strength of the steels [30,31]. The increased amounts of MX in the CNAs reduce the amount of $M_{23}C_6$ in the CNA1 and even more in the CNA2 and CNA3 as compared with Eurofer97. Additionally, the amount of Laves phase in the CNAs was designed to be similar to that in Eurofer97.

Table 1. Chemical compositions (wt%) of the iron-based alloys*

| | 9Cr FM steels | | 9Cr RAFM Steels | | | | 9Cr CNAs | | | 9–20Cr NFA/ODS | | | |
|---|---|---|---|---|---|---|---|---|---|---|---|---|---|
| | G91 [2] | G92 [2] | JFL-1 [1] | F82H [1] | E97 [1] | CLAM [32] | CNA1 (this work) | CNA2 (this work) | CNA3 (this work) | ODS-E [8] | MA956 [9] | PM2000 [9] | 14YWT [10] |
| C | 0.09 | 0.11 | 0.1 | 0.1 | 0.11 | 0.1 | 0.1 | 0.1 | 0.1 | 0.11 | | | |
| N | 0.04 | 0.05 | 0.05 | 0.01 | 0.03 | | 0.06 | 0.003 | 0.004 | | | | |
| Cr | 8.7 | 9.3 | 9 | 8 | 9 | 8.9 | 9 | 8.6 | 8.6 | 8.9 | 20 | 20 | 14 |
| Mn | 0.35 | 0.41 | 0.45 | 0.3 | 0.4 | 0.45 | 0.5 | 0.5 | 1 | 0.42 | | | |
| V | 0.22 | 0.16 | 0.19 | 0.2 | 0.2 | 0.2 | 0.3 | 0.2 | 0.1 | 0.2 | | | |
| W | | 1.67 | 2 | 2 | 1.1 | 1.5 | 1.1 | 1.3 | 1.3 | 1.1 | | | 3 |
| Ta | | | 0.07 | 0.04 | 0.07 | 0.15 | 0.14 | 0.1 | 0.1 | 0.14 | | | |
| Si | 0.29 | 0.1 | <0.1 | 0.1 | 0.04 | 0.1 | 0.25 | 0.1 | 0.15 | 0.06 | | | |
| Other | 0.07Nb; 0.9Mo; 0.28Ni | 0.06Nb; 0.42Mo; 0.17Ni | | | | | | 0.15Ti | 0.15Ti | $0.3Y_2O_3$ | 4.5Al; 0.5Ti; $0.5Y_2O_3$ | 5.5Al; 0.5Ti; $0.5Y_2O_3$ | 0.4Ti; $0.3Y_2O_3$ |

* The abbreviated names of G91, G92, E97, and ODS-E are Grade 91, Grade 92, Eurofer97, and ODS-Eurofer, respectively. The blanket cells denote that values are not available/reported because of their low impurity levels.

Fig. 3b and 3c compare the calculated equilibrium vol% of $M_{23}C_6$, Laves, MX, and Z phases in the two CNAs to those in the two current RAFM steels F82H and Eurofer97 at 760 (tempering) and 650°C, respectively. The CNAs possess ~0.4–0.5 vol% MX, which is lower than the oxide nanoclusters (>~0.7 vol%) in the 9–20Cr ODS alloys, but significantly higher than the MX (<0.2 vol%) in F82H and Eurofer97.

According to the experimental coarsening kinetics of $M_{23}C_6$ and MX precipitates as shown in Fig. 3d [6], together with the calculated equilibrium vol% of the phases in Fig. 3b-c, the strength of the alloys at specific temperatures can be estimated using the back-stress concept [33]. Laves phase coarsening kinetics is not included in Fig. 3d because of its absence at the studied temperature of 650°C. The following equations give the primary strengthening components of free dislocations ($\Delta\sigma_{disl}$), precipitates ($\Delta\sigma_{ppt}$), subgrain boundaries ($\Delta\sigma_{sgb}$), and grain boundaries ($\Delta\sigma_{gb}$):

$$\Delta\sigma_{disl} \approx C_1 MGb\sqrt{\rho_m},$$

$$\Delta\sigma_{ppt} \approx \alpha MGb\sqrt{Nd},$$

$$\Delta\sigma_{sgb} \approx MGb/\lambda_{sgb},$$

$$\Delta\sigma_{gb} \approx \beta MGb/\sqrt{d_g}.$$

Definitions of the parameters are: the constant $C_1 = 0.5$ [34], Taylor factor $M \approx 2.9$ for ferritic steels [35], shear modulus $G \approx 80.8$ and 57.7 GPa at 25 and 650°C, respectively, Burgers vector $b \approx 0.25$ nm, mobile dislocation density $\rho_m$ on the order of $10^{14}$ $m^{-2}$ in the initial as-fabricated condition, strength factor $\alpha \approx 0.1757ln(2.7013d)$ [ 36 ], number density $N$ ($m^{-3}$) and size/diameter $d$ (nm) of precipitates, the width of the lath/subgrain boundaries $\lambda_{sgb}$, the constant $\beta \approx 4380$ $m^{-1/2}$ [37], and the grain size/diameter $d_g$. The time-dependent precipitate strengthening effect calculated from these equations according to the results of Fig. 3b-d is shown in Fig. 3e for the two CNAs and for Eurofer97. The root-sum-square law of $\Delta\sigma_{ppt} = \sqrt{\sum_i \Delta\sigma_{ppt,i}^2}$ or in combination with the linear law of $\Delta\sigma_{ppt} = \sum_i \Delta\sigma_{ppt,i}$ was employed to integrate comparable or dissimilar contributions from different types ($i$) of precipitates, respectively. As compared to the retained strength in the CNA2, the transformation to Z-phase from MX resulted in rapid strength

reduction in the CNA1 and Eurofer97. Using these type of rough estimations, promising CNAs were down-selected for experimental studies.

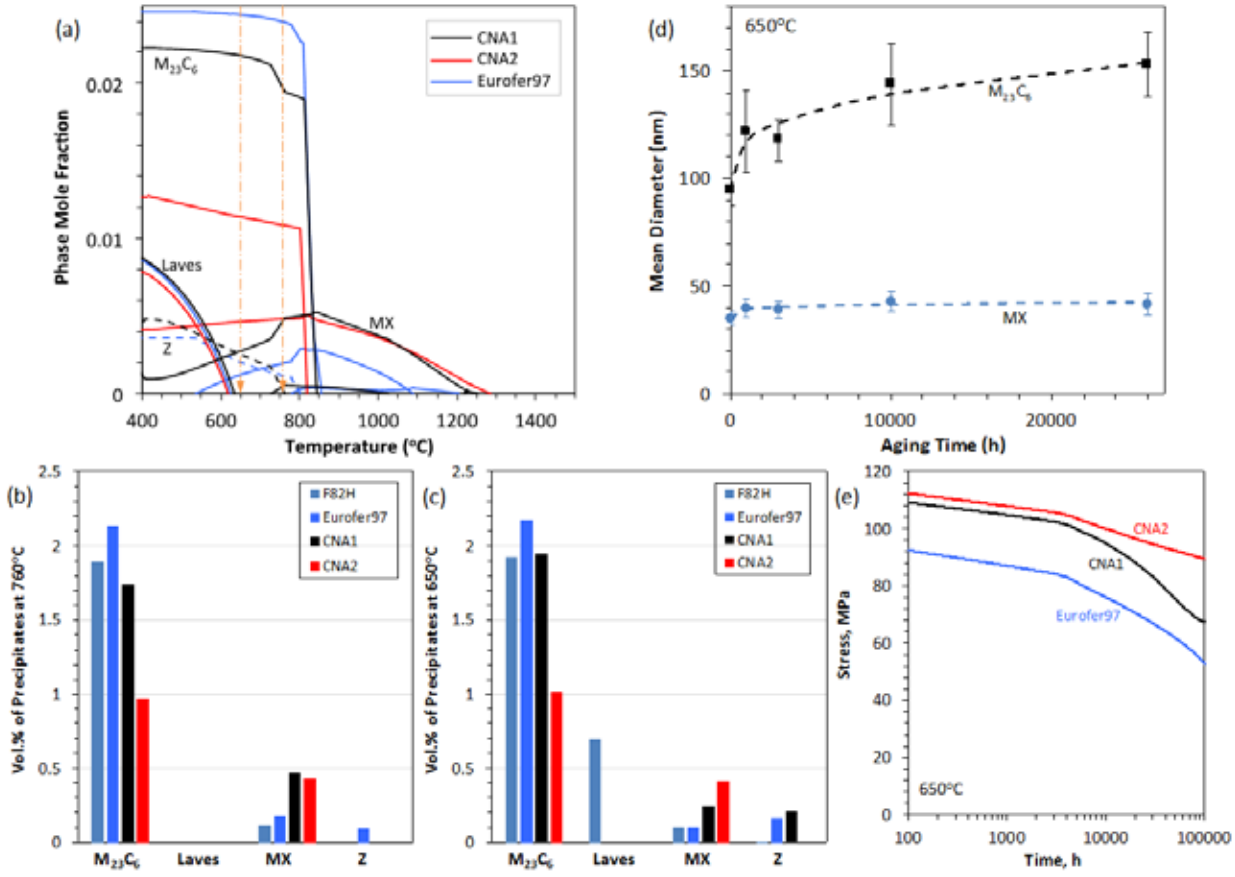


Fig. 3. Alloy design through computational alloy thermodynamics (a-c) and experimental precipitate coarsening kinetics (d) for the estimation of precipitate strengthening (e).

## 3. Experimental methods

Small laboratory heats of ~0.7 kg of all the CNAs were manufactured by arc-melting and drop-casting in an argon atmosphere and hot-rolling in air to 8 mm thick plate, followed by normalization at 1120°C for 20 minutes and tempering at 750°C for 30 minutes then air cooled. Microstructures of the alloys were characterized using optical microscopy, transmission electron microscopy (TEM) on a Philips CM200 field emission gun microscope at 200 kV, integrated with

scanning-mode TEM (STEM) and energy dispersive x-ray spectroscopy (EDS). Focused ion beam (FIB: Hitachi NB5000) was used to lift-out and thin TEM specimens. The mechanical properties of the alloys were measured in air with tensile tests up to 800°C at a strain rate of $3\times10^{-4}$ $s^{-1}$, creep tests at 600 and 650°C, and Charpy impact tests. Type SS-3 miniature tensile specimens (25.4 × 4.95 × 0.76 mm with a gauge section of 7.62 × 1.52 × 0.76 mm), machined along the rolling direction of the plates, were used for the tensile and creep tests. Half-size Charpy impact specimens (5 × 5 × 25.4 mm with a 1 mm deep V-notch) were tested to determine upper-shelf energy (USE) and DBTT of the alloys. The T–L (transverse–longitudinal) specimen orientation with cracking plan parallel to the longitudinal (i.e., rolling direction) was primarily tested since this orientation was confirmed to give the worse impact resistance (i.e., lower USE and higher DBTT) compared to the L–T specimen orientation in screening tests.

## 4. Results and discussion

Figure 4 shows an example microstructure of the CNA2, illustrating common tempered martensite structure with varied packets/blocks in the optical image (Fig. 4a), lath width in the range of ~100 to 400 nm in the bright-field (BF) TEM image (Fig. 4b), and high densities of ultrafine MX precipitates (~7 nm and ~$2\times10^{22}$ $m^{-3}$) and free dislocations (~$3\times10^{14}$ $m^{-2}$) in the BF STEM image (Fig. 4c). The amount of MX precipitates in the CNA2 was estimated to be <~0.36 vol% accordingly, which is less than the thermodynamic calculation predicted 0.42 vol% in Fig. 3b. The discrepancy may be attributable to variable distribution of the precipitates and more likely the possible presence of complex Ta/Ti-bearing oxides as previously reported in the CNA1 type steel [22], which compromised the available Ta/Ti for MX formation. Thorough microstructural characterization will be pursued to have better statistical results and identify other forms of phases

containing Ta and/or Ti. Compared to the generally reported MX nanoprecipitates of ~30 nm on the order of $10^{20}$ $m^{-3}$ (comparable to the calculated 0.17 vol% in Fig. 3b) and lath width of ~200–500 nm in Eurofer97 [38], the CNA2 has noticeably finer nanoprecipitates with density increased up to two orders of magnitude, as well as a refined lath structure.

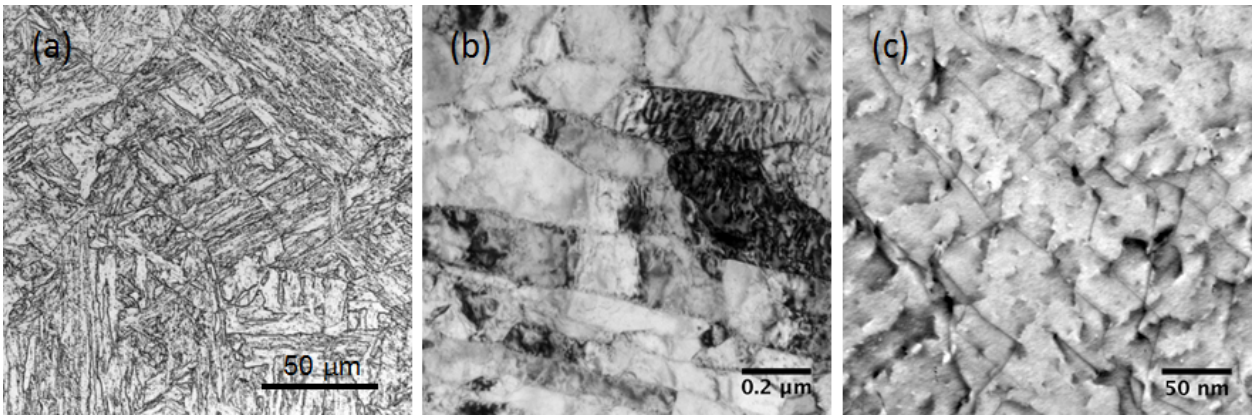


Fig. 4. (a) Optical, (b) BF-TEM, and (c) BF-STEM images showing microstructures of the CNA2.

According to the microstructural results derived from experiments of this work for CNA2 and literature for CNA1, 9Cr RAFM steels, and 9–20Cr NFA/ODS alloys [8,9,10,22,29,32,38,39,40] and calculated vol%, microstructural components, i.e., coarse/fine particles, dislocations, and subgrains/grains, in the as-fabricated condition of these alloys are summarized in Table 2. It includes the calculated strengthening contributions ($\Delta\sigma_{disl}$, $\Delta\sigma_{ppt}$, $\Delta\sigma_{sgb}$, and $\Delta\sigma_{gb}$ according to the equations in Section 2) to the total strength of the alloys at room temperature. The comparison indicates that:

a) Dislocations are the primary strengthening component in RAFM steels and CNAs, which suffers recovery at elevated temperatures.

b) The superior strength of NFA/ODS alloys is attributable primarily to the predominant fine oxide nanoclusters, with some contribution from the small grain size. Although extremely

high dislocation density was reported in ODS alloys after thermomechanical treatment [40], which could yield as high as ~800 MPa strengthening, lower dislocation densities, corresponding to ~180–400 MPa, were usually used to produce a better balance of properties.

c) With the CNA2 as an example, the MX particles (~7 nm and ~$2\times10^{22}$ $m^{-3}$), dislocations (~$3\times10^{14}$ $m^{-2}$), lath subgrains (~400 nm in average), and prior-austenite grains (~50 μm) would approximately produce 358, 507, 146, and 36 MPa strengthening, respectively. Statistical experimental data of $M_{23}C_6$ were not obtained from the FIB-ed specimens of CNA2, which could be estimated to be 100 nm and $2\times10^{19}$ $m^{-3}$, corresponding to 81 MPa strengthening. The total strengthening from these microstructural components in CNA2 is estimated to be 727 MPa using the root-sum-square law in combination with the linear law. Compared to RAFM steels, the enhanced strength of CNAs is primarily attributable to the significantly increased concentration of MX nanoprecipitates that provide a strengthening effect similar to the lower bound of the fine oxide nanocluster hardening in NFA/ODS alloys. Further increasing the amount of MX nanoprecipitates would be challenging because alloying with additional MX formers would destabilize austenite at high temperatures.

Table 2. Comparison of microstructural components and estimated strengthening contributions at room temperature for 9Cr RAFM steels, 9Cr CNAs, and 9–20Cr NFA/ODS alloys in the as-fabricated condition.

| Microstructure | | 9Cr RAFM steels [38,39] | 9Cr CNAs [22,29, this work] | 9–20Cr NFA/ODS alloys [8,9,10,32,40] |
|---|---|---|---|---|
| Coarse particles | Size, nm | ~70–300 ($M_{23}C_6$, TaN, etc.) | ~70–150 ($M_{23}C_6$, TaN, etc.) | ~50–100 (singular/agglomerated oxide clusters, TiN, $M_{23}C_6$, etc.) |

| | | | | |
|---|---|---|---|---|
| | Density, $m^{-3}$ | $10^{18}$ to $10^{19}$ | $10^{18}$ to $10^{19}$ | $10^{18}$ |
| | vol% (cal.) | ~2 | ~0.9–1.8 | <~0.1 |
| | $\Delta\sigma_{ppt}$, MPa | ~40–140 | ~50–140 | ~20–40 |
| Fine particles | Size, nm | ~10–50 (MX, etc.) | ~3–20 (MX, etc.) | ~2–30 (oxide nanoclusters, etc.) |
| | Density, $m^{-3}$ | $10^{19}$ to $10^{20}$ | $10^{21}$ to $10^{22}$ | $10^{21}$ to $10^{24}$ |
| | vol% (cal.) | <0.2 | ~0.4–0.6 | ~0.7–3 |
| | $\Delta\sigma_{ppt}$, MPa | ~60–140 | ~180–500 | ~300–1200 |
| Dislocations | Density, $m^{-2}$ | $\sim 2\times10^{14}$ | $\sim 3\times10^{14}$ | $\sim(0.1–7.8)\times10^{14}$ |
| | $\Delta\sigma_{disl}$, MPa | ~400 | ~500 | ~90–800 |
| Lath subgrains | Width, nm | ~200–500 | ~100–500 | ~200–500 (only in 9Cr) |
| | $\Delta\sigma_{sgb}$, MPa | ~120 | ~150 | ~120 (only in 9Cr) |
| Grains | Size, μm | ~10–60 (prior-austenite) | ~10–60 (prior-austenite) | ~0.4–2 |
| | $\Delta\sigma_{gb}$, MPa | ~30–80 | ~30–80 | ~180–400 |
| Total Strength ($\Delta\sigma$)* | | <~500 | <~700 | ~520–1500 |

* Total strength (not including the intrinsic strength of the alloy matrix from solid solution and lattice friction strengthening) was estimated from the strengthening components in each alloy of Table 1 according to the root-sum-square law $\Delta\sigma = \sqrt{\sum_{m,i} \Delta\sigma_{m,i}^2}$ or in combination with the linear law $\Delta\sigma = \sum_{m,i} \Delta\sigma_{m,i}$ for the *m* types of microstructural components and *i* types of species (e.g., precipitates).

The temperature-dependent yield stress and total elongation of the CNAs are shown in Fig. 5. The results are compared with literature data for F82H [41], Eurofer97 [42], P91 [2], and PM2000 ODS alloy [43]. The yield strength of the CNAs was ~100–300 MPa higher than the RAFM/FM steels at the test temperatures, and even comparable or slightly superior to PM2000 at temperatures above ~500°C. The yield strength of the CNA2 (~783 MPa) at room temperature is greater than the calculated strengthening of 727 MPa from the microstructural components. The higher test strength suggests the role of intrinsic strength of the alloy on the level of 270 MPa according to the root-sum-square law, which is approximately consistent with the intrinsic strength of 261 MPa for 13.5Cr–1.1W–0.3Ti [40]. The higher strength of the CNAs was achieved at the cost of some reductions in total elongation, which is lower than the RAFM/FM steels and comparable or superior to PM2000. It should be noted here that the tensile properties of the CNAs were determined using type SS-3 miniature specimens with a rectangular gauge cross-section of 1.52 × 0.76 $mm^2$, in contrast to the large round gauge cross-section specimens of Eurofer97 and P91 with

area 19.6 mm$^2$ [42] and 78.5 mm$^2$ [2], respectively. The limited deformation volume of the SS-3 miniature specimens could somewhat decrease their ductility.

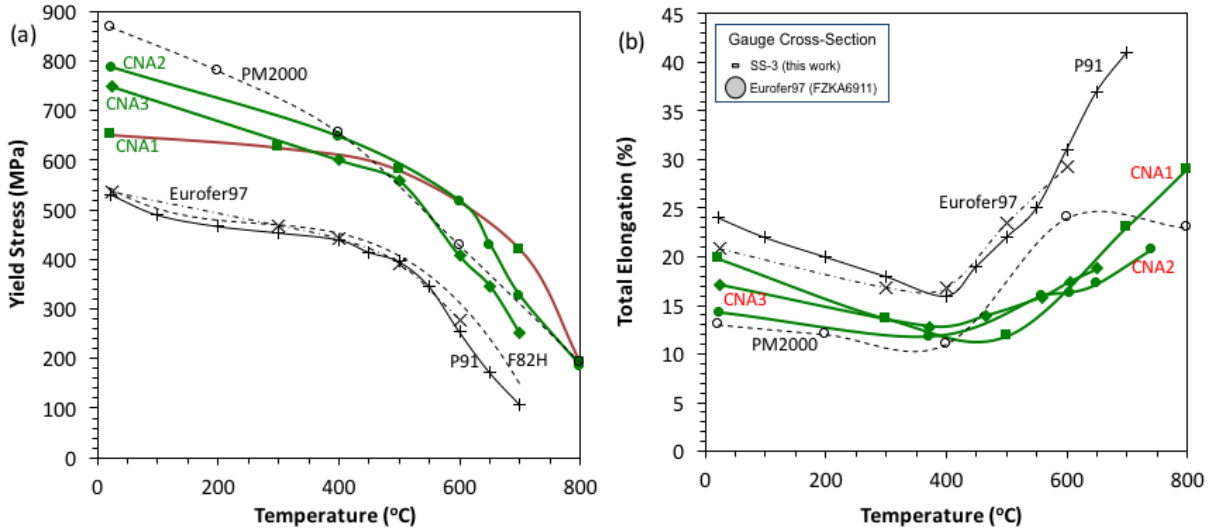


Fig. 5. Temperature-dependent yield strength and total elongation of CNAs compared to F82H [41], Eurofer97 [42], P91 [2], and PM2000 [43].

Preliminary creep test results for the CNAs are shown in Fig. 6 with creep rupture stress as a function of Larson-Miller parameter (LMP) $T(30+\log t_r)/1000$, where $T$ and $t_r$ are temperature in K and time to rupture in h, respectively. Comparing to the literature data of F82H [41], Eurofer97 [42], JLF-1 [32], CLAM [32], and ODS-Eurofer [44,45] in Fig. 6, the CNAs show creep resistance superior to the RAFM steels (F82H, Eurofer97, JLF-1 and CLAM), while approaching the lower bound of the data scatter for ODS-Eurofer. The improvement in creep resistance of the CNAs was getting smaller at lower stresses (or higher temperatures or longer times). The creep lives of the CNA2 tested at 110 MPa and 650°C in air were up to 581 h, with minimum creep rates as low as $2.2\times10^{-5}$ h$^{-1}$ and creep elongations of ~20%. In comparison, Eurofer97 exhibited comparable creep lives and minimum creep rates, but higher creep elongations (~30–40% depending on different thermomechanical treatments) at 80–100 MPa and 650°C in vacuum [42]. The lower

creep elongations of the CNA2 may have been compromised by its higher creep strength and high-temperature oxidation of the type SS-3 miniature specimens. Larger heats of CNAs are being manufactured; creep tests will be repeated on regular-size samples, comparable to those used in the F82H and Eurofer97 tests.

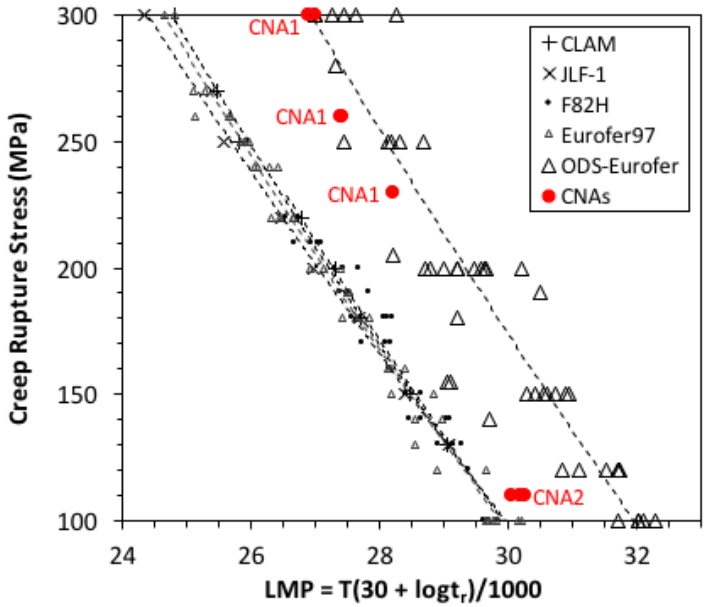


Fig. 6. Larson-Miller creep parameter plot for CNAs compared with RAFM steels (i.e., CLAM, JLF-1, F82H, and Eurofer97) and ODS-Eurofer alloy.

Charpy impact test data for CNAs, together with literature data for Grade 91 [46], Eurofer97 and 9–20Cr ODS alloys [47], all in the T–L sample orientation, are shown in Fig. 7 as absorbed energy as a function of test temperature. The Eurofer97 (open circles) and 9–20Cr ODS alloys, including ODS-Eurofer (dash signs), PM2000 (plus signs), and MA956 (crosses), were tested using KLST specimens with dimensions 3 × 4 × 27 mm with 1 mm notch depth. The T–L orientation refers to transverse–extrusion orientation for ODS alloys. The absorbed energy is normalized to the area under the notch of the specimens, shown in the shaded area of the inset in Fig. 7. To obtain DBTT and USE, the data were fitted by a hyperbolic tangent function $E = a + b$

tanh[$(T - T_0)/c$], where $T$ is test temperature and $a$, $b$, $c$ and $T_0$ are regression coefficients. $T_0$ gives the mathematical DBTT, corresponding to the mean value of USE and lower-shelf energy (LSE), i.e., 1/2USE assuming LSE = 0 in Fig. 7. The results indicate that CNA1 has USE and DBTT comparable to Grade 91, with comparable or lower DBTT and about two times greater USE than the 9–20Cr ODS alloys. Eurofer97 exhibited both lower USE and DBTT than Grade 91. However, DBTT comparison between the Eurofer97 and CNAs/Grade 91 data is not reliable because smaller specimens (e.g., KLST) tend to yield lower DBTT than larger specimens in Charpy impact tests. Compared to Grade 91, the CNA2 and CNA3 exhibited remarkable increase in USE with comparable or lower DBTT. Smaller precipitates have been demonstrated to have a beneficial effect of lowering DBTT and improving absorbed energy in bainitic and tempered martensitic steels [48,49]. The refined precipitates and subgrain structures shown in Fig. 4, together with the adjusted alloy content of Mn, Si, and V, may have contributed to noticeably improving the Charpy impact toughness of the CNAs. Despite the fine grains in the range of ~0.4–2 μm, together with the high density of fine oxide clusters listed in Table 2, ODS alloys exhibited noticeably lower impact toughness, which is attributable to the delamination of the heterogeneous microstructure inherited from the MA fabrication method [50], resulting in an impact fracture mechanism different from RAFM/FM steels.

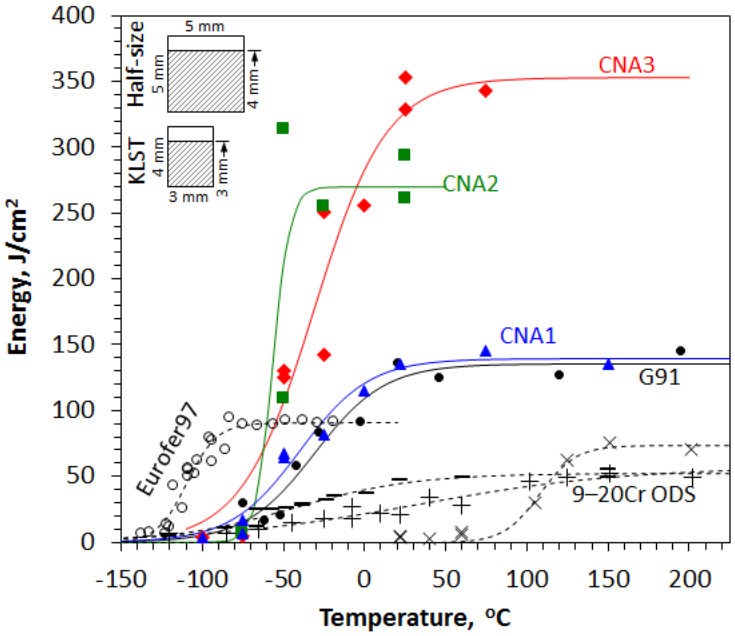


Fig. 7. Charpy impact toughness of CNAs compared with Grade 91 (half-size), Eurofer97 and 9–20Cr ODS alloys (KLST).

Comparing the measured USE, the estimated total strength ($\Delta\sigma$ in Table 2) and sink strength ($S$, e.g., Fig. 2), the dependence of USE and $S$ on $\Delta\sigma$ for the three groups of alloys is schematically shown in Fig. 8. The 9Cr RAFM steels, including conventional 9Cr FM, have the lowest $\Delta\sigma$ with a moderate range of USE. The 9–20Cr ODS/NFA steels have the highest $\Delta\sigma$ but the lowest USE. The 9Cr CNAs possess significant increases in $\Delta\sigma$ with noticeably improved USE. As discussed in connection with Table 2, the $\Delta\sigma$ is attributed to particles, dislocations, and boundaries, and these are the primary elements in determining $S$. While the data on radiation resistance is still scant, the CNAs with noticeably increased amount of MX nanoprecipitates are expected to have radiation resistance and helium management performance superior to current RAFM steels because of the increased defect sinks at the nanoparticle-matrix interface. The relationship of $\Delta\sigma^2 \propto S$ can be deduced by correlating the strengthening equations in Section 2 with the descriptive equations for

the sink strength of the primary elements [11]. Therefore, the general increases of $S$ with increasing $\Delta\sigma$ are schematically denoted with dotted lines in logarithmic scales of Fig. 8. The 9Cr CNAs having noticeably increased $S$, USE, and $\Delta\sigma$ are expected to have promising applications for fusion and fission reactor components compared to both 9Cr RAFM/FM and 9–20Cr NFA/ODS.

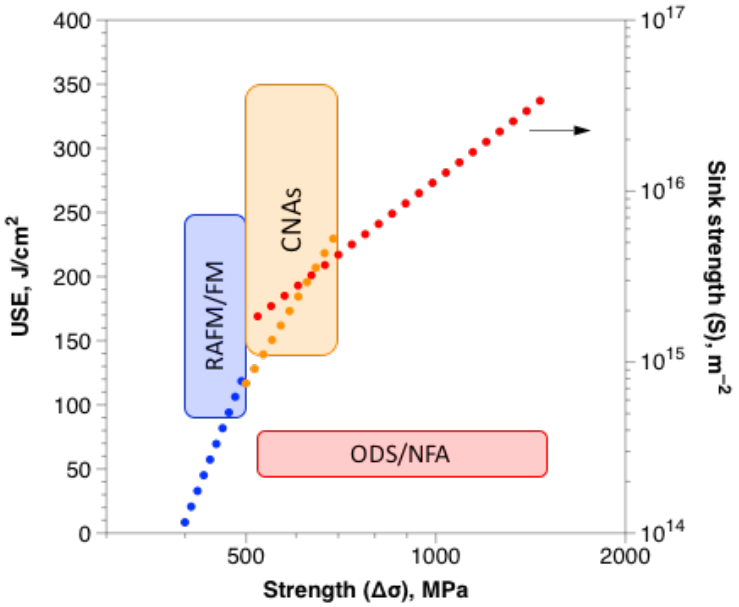


Fig. 8. Schematic dependence of USE and sink strength on the estimated total strength of 9Cr RAFM/FM (blue), 9Cr CNAs (orange), and 9–20Cr NFA/ODS (red).

## 5. Conclusions

A new generation of RAFM steels, named as CNAs, has been manufactured using traditional steelmaking methods. These alloys were designed and manufactured to retain a high density of stable ultrafine nanoprecipitates, predicted to result in high temperature strength and improved radiation resistance compared to current RAFM steel. Computational alloy thermodynamics coupled with strength modeling was used to design CNAs, which are strengthened primarily by either MN or MC nanoprecipitates. The amount of MN or MC was designed to be ~0.4–0.6 vol%

in the CNAs, which is lower than the oxide nanocluster content (>~0.7 vol%) in the 9–20Cr ODS alloys, but significantly higher than the MX (<0.2 vol%) in current RAFM steels. The experimental heat of CNA2 demonstrated significantly refined MX nanoprecipitates (~7 nm) with a high density (~$2\times10^{22}$ $m^{-3}$), as well as a refined subgrain structures and a high density of free dislocations (~$3\times10^{14}$ $m^{-2}$), leading to improvements in strength, creep resistance, and Charpy impact toughness.

The CNAs exhibited ~100–300 MPa higher yield strength than the RAFM/FM steels at test temperatures up to 800°C, and comparable or slightly superior strength to PM2000 at temperatures above ~500°C. The enhanced strength was achieved at the cost of a modest reduction in ductility. Preliminary creep tests indicated superior creep resistance compared to RAFM steels, which approached the lower bound of the scatter data of ODS-Eurofer. The CNAs showed Charpy impact toughness comparable to or significantly greater than Grade 91, in terms of higher USE and lower DBTT. The improvement levels were even greater when compared to 9–20Cr ODS alloys.

**Acknowledgment**

This research was supported by the U.S. Department of Energy, Office of Science, Fusion Energy Sciences and Office of Nuclear Energy, Nuclear Energy Enabling Technology FY 2012 Award. This manuscript has been authored by UT-Battelle, LLC, under Contract No. DE-AC05-00OR22725 with the U.S. Department of Energy.

The authors appreciate Eric Manneschmidt for his consistent help on mechanical tests and S.J. Zinkle, F.W. Wiffen and A. Rowcliffe for helpful discussions.

**References**

[1] A. Kohyama, A. Hishinuma, D.S. Gelles, R.L. Klueh, W. Dietz, K. Ehrlich, Low-activation ferritic and martensitic steels for fusion application, J. Nucl. Mater. 233–237 (1996) 138–147.
[2] NIMS Creep Data Sheet No. 43A (Grade 91), 2014; No. 48A (Grade 92), 2012, National Institute for Materials Science, Japan.
[3] R.L. Klueh, E.T. Cheng, M.L. Grossbeck, E.E. Bloom, Impurity effects on reduced-activation ferritic steels developed for fusion applications, J. Nucl. Mater. 280 (2000) 353–359.
[4] K. Kimura, H. Kushima, F. Abe, Heterogeneous changes in microstructure and degradation behavior of 9Cr-1Mo-V-Nb steel during long term creep, Key Eng. Mater. 171–174 (2000) 483–490.
[5] L. Tan, T.S. Byun, Y. Katoh, L.L. Snead, Stability of MX-type strengthening nanoprecipitates in ferritic steels under thermal aging, stress and ion irradiation, Acta Mater. 71 (2014) 11–19.
[6] Å. Gustafson, M. Hättestrand, Coarsening of precipitates in an advanced creep resistant 9% chromium steel–quantitative microscopy and simulations, Mater. Sci. Eng. A 333 (2002) 279–286.
[7] G.R. Odette, M.J. Alinger, B.D. Wirth, Recent developments in irradiation-resistant steels, Annu. Rev. Mater. Res. 38 (2008) 471–503.
[8] C. Heintze, F. Bergner, A. Ulbricht, M. Hernández-Mayoral, U. Keiderling, R. Lindau, T. Weissgärber, Microstructure of oxide dispersion strengthened Eurofer and iron–chromium alloys investigated by means of small-angle neutron scattering and transmission electron microscopy, J. Nucl. Mater. 416 (2011) 35–39.
[9] A. Wasilkowska, M. Bartsch, U. Messerschmidt, R. Herzog, A. Czyrska-Filemonowicz, Creep mechanisms of ferritic oxide dispersion strengthened alloys, J. Mater. Process. Tech. 133 (2003) 218–224.
[10] A. Hirata, T. Fujita, C.T. Liu, M.W. Chen, Characterization of oxide nanoprecipitates in an oxide dispersion strengthened 14YWT steel using aberration-corrected STEM, Acta Mater 60 (2012) 5686–5696.
[11] S.J. Zinkle, L.L. Snead, Designing radiation resistance in materials for fusion energy, Annu. Rev. Mater. Res. 44 (2014) 241–267.
[12] L. Tan, J.T. Busby, P.J. Maziasz, Y. Yamamoto, Effect of thermomechanical treatment on 9Cr ferritic-martensitic steels, J. Nucl. Mater. 441 (2013) 713–717.
[13] M. Taneike, F. Abe, K. Sawada, Creep-strengthening of steel at high temperatures using nano-sized carbonitrides dispersions, Nature 424 (2003) 294–296.
[14] V. Shankar, K. Mariappan, A. Nagesha, G.V. Prasad Reddy, R. Sandhya, M.D. Mathew, T. Jayakumar, Effect of tungsten and tantalum on the low cycle fatigue behavior of redueced activation ferritic/martensitic steels, Fus. Eng. Des. 87 (2012) 318–324.
[15] F. Abe, Strengthening mechanisms in creep of advanced ferritic power plant steels based on creep deformation analysis, in: Y. Weng, H. Dong, Y. Gan (Eds.), Advanced Steels, Springer-Verlag Berlin Heidelberg and Metallurgical Industry Press, 2011, p.409–422.
[16] F. Abe, H. Araki, T. Noda, The effect of tungsten on dislocation recovery and precipitation behavior of low-activation martensitic 9Cr steels, Metall. Trans. A 22 (1991) 2225–2235.
[17] K. Laha, S. Saroja, A. Moitra, R. Sandhya, D.M. Mathew, T. Jayakumar, E.R. Kumar, Development of India-specific RAFM steel through optimization of tungsten and tantalum contents for better combination of impact, tensile, low cycle fatigue and creep properties, J. Nucl. Mater. 439 (2013) 41–50.

[18] J. Vanaja, K. Laha, M. Nandagopal, S. Sam, M.D. Mathew, T. Jayakumar, E.R. Kumar, Effect of tungsten on tensile properties and flow behavior of RAFM steel, J. Nucl. Mater. 433 (2013) 412–418.
[19] F. Abe, Effect of fine precipitation and subsequent coarsening of $Fe_2W$ Laves phase on the creep deformation behavior of tempered martensitic 9Cr-W steels, Metall. Mater. Trans. A 36 (2005) 321–332.
[20] Y. de Carlan, A. Alamo, M.H. Mathon, G. Gepffroy, A. Castaing, Effect of thermal aging on the microstructure and mechanical properties of 7–11 CrW steels, J. Nucl. Mater. 283–287 (2000) 672–676.
[21] T. Hasegawa, Y. Tomita, A. Kohyama, Influence of tantalum and nitrogen contents, normalizing condition and TMCP process on the mechanical properties of low-activation 9Cr–2W–0.2V–Ta steels for fusion application, J. Nucl. Mater. 258–263 (1998) 1153–1157.
[22] L. Tan, Y. Yang, J.T. Busby, Effects of alloying elements and thermomechanical treatment on 9Cr reduced activation ferritic-martensitic (RAFM) steels, J. Nucl. Mater. 442 (2013) S13–S17.
[23] V. Shankar, K. Mariappan, R. Sandhya, K. Laha, T. Jayakumar, E. Rajendra Kumar, Effect of W and Ta on creep-fatigue interaction behavior of reduced activation ferritic-martensitic (RAFM) steels, Fus. Eng. Des. 100 (2015) 314–320.
[24] S. Chen, L. Rong, Effect of silicon on the microstructure and mechanical properties of reduced activation ferritic/martensitic steel, J. Nucl. Mater. 459 (2015) 13–19.
[25] Y. Hosoi, N. Wade, S. Kunimitsu, T. Urita, Precipitation behavior of Laves phase and its effect on toughness of 9Cr-2Mo ferritic-martensitic steel, J. Nucl. Mater. 141–143 (1986) 461–467.
[26] Pandat software <http://www.computherm.com>.
[27] Y. Yang, J.T. Busby, Thermodynamic modeling and kinetics simulation of precipitate phases in AISI 316 stainless steels, J. Nucl. Mater. 448 (2014) 282–293.
[28] R.L.Klueh, Reduced activation status: future development for improved creep strength, J. Nucl. Mater. 378 (2008) 159–166.
[29] L. Tan, D.T. Hoelzer, J.T. Busby, M.A. Sokolov, R.L. Klueh, Microstructure control for high strength 9Cr ferritic-martensitic steels, J. Nucl. Mater. 422 (2012) 45–50.
[30] L. Cipolla, H.K. Danielsen, D. Venditti, P.E.D. Nunzio, J. Hald, M.A.J. Somers, Conversion of MX nitrides to Z-phase in a martensitic 12% Cr steel, Acta Mater. 58 (2010) 669–679.
[31] K. Sawada, H. Kushima, M. Tabuchi, K. Kimura, Effect of creep deformation on Z phase formation in Gr.91 steel, Mater. Sci. Tech. 30 (2014) 12–16.
[32] Y. Li, T. Nagasaka, T. Muroga, A. Kimura, S. Ukai, High-temperature mechanical properties and microstructure of 9Cr oxide dispersion strengthened steel compared with RAFMs, Fus. Eng. Des. 86 (2011) 2495–2499.
[33] E. Kozeschnik, I. Holzer, Precipitation during heat treatment and service: characterization, simulation and strength contribution, in: F. Abe, T.-U. Kern, R. Viswanathan (Eds.), Creep-Resistant Steels, Woodhead Publishing Limited, Cambridge, England, 2008.
[34] K. Maruyama, K. Sawada, J. Koike, Strengthening mechanisms of creep resistant tempered martensitic steel, ISIJ Inter. 41 (2001) 641–653.
[35] U.F. Kocks, The relation between polycrystals deformation and single-crystal deformation, Met. Trans. 1 (1970) 1121–1143.
[36] L. Tan, J.T. Busby, Formulating the strength factor $\alpha$ for improved predictability of radiation hardening, J. Nucl. Mater. 465 (2015) 724–730.

[37] C.C. Eiselt, Eigenschaftsoptimierung der nanoskaligen ferritischen ODS-Legierung 13Cr-1W-0.3$Y_2O_3$-0.3$TiH_2$, metallkundliche Charakterisierung und Bestimmung von Struktur-Eigenschaftskorrelationen. Vol. FZKA Report 7524. Karlsruhe: Karlsruhe Institute of Technology, 2010.
[38] M. Klimenkov, R. Lindau, E. Materna-Morris, A. Möslang, TEM characterization of precipitates in Eurofer 97, Prog. Nucl. Ener. 57 (2012) 8–13.
[39] C. Dethloff, E. Gaganidze, J. Aktaa, Quantitative TEM analysis of precipitation and grain boundary segregation in neutron irradiated Eurofer97, J. Nucl. Mater. 454 (2014) 323–331.
[40] P. He, On the structure-property correlation and the evolution of nanofeatures in 12–13.5% Cr oxide dispersion strengthened ferritic steels, Karlsruher Institute für Technology, 2014.
[41] A.-A.F. Tavassoli, J.W. Rensman, M. Schirra, K. Shiba, Materials design data for reduced activation martensitic steel type F82H, Fus. Eng. Des. 61–62 (2002) 617–628.
[42] M. Rieth, M. Schirra, A. Falkenstein, P. Graf, S. Heger, H. Kempe, R. Lindau, H. Zimmermann, Eurofer 97 tensile, Charpy, creep and structural tests, Forschungszentrum Karlsruhe in der Helmholtz-Gemeinschaft, Wissenschaftliche Berichte FZKA 6911, October 2003.
[43] R.L. Klueh, J.P. Shingledecker, R.W. Swindeman, D.T. Hoelzer, Oxide dispersion-strengthened steels: a comparison of some commercial and experimental alloys, J. Nucl. Mater. 341 (2005) 103–114.
[44] R. Lindau, A. Möslang, M. Rieth, M. Klimiankou, E. Materna-Morris, A. Alamo, A.-A.F. Tavassoli, C. Cayron, A.M. Lancha, P. Fernandez, N. Baluc, R. Schäublin, E. Diegele, G. Filacchioni, J.W. Rensman, B. van der Schaaf, E. Lucon, W. Dietz, Present development status of Eurofer and ODS-Eurofer for application in blanket concepts, Fus. Eng. Des. 75–79 (2005) 989–996.
[45] G. Yu, N. Nita, N. Baluc, Thermal creep behavior of the Eurofer 97 RAFM steel and two European ODS Eurofer 97 steels, Fus. Eng. Des. 75–79 (2005) 1037–1041.
[46] W.R. Corwin, A.M. Hougland, Effect of specimen size and material condition on the Charpy impact properties of 9Cr-1Mo-V-Nb steel, in: W.R. Corwin, G.E. Lucas (Eds.), The Use of Small-Scale Specimens for Testing Irradiated Material, ASTM STP 888, American Society for Testing and Materials, Philadelphia, 1986, p. 325.
[47] P. Fernández, M. Serrano, J. Lapeña, Metallurgical comparison between the experimental EU-ODS and commercial ODS steels, International Conference on Fusion Reactor Materials (ICFRM-13), Nice, France, 10-14 Dec. 2007.
[48] Y.-R. Im, Y.J. Oh, B.-J. Lee, J.H. Hong, H.-C. Lee, Effects of carbide precipitation on the strength and Charpy impact properties of low carbon Mn–Ni–Mo bainitic steels, J. Nucl. Mater. 297 (2001) 138–148.
[49] S. Takebayashi, K. Ushioda, N. Yoshinaga, S. Ogata, Effect of carbide size distribution on the impact toughness of tempered martensitic steels with two different prior austenite grain sizes evaluated by instrumented Charpy test, Mater. Trans. 54 (2013) 1110–1119.
[50] J. Chao, C. Capdevila, M. Serrano, A. Garcia-Junceda, J.A. Jimenez, G. Pimentel, E. Urones-Garrote, Notch impact behavior of oxide-dispersion-strengthened (ODS) Fe20Cr5Al alloy, Metall. Mater. Trans. A 44 (2013) 4581–4594.